XLVI CILAMCE
VITÓRIA - ES - BRAZIL - 2025
XLVI IBERO-LATIN AMERICAN CONGRESS ON COMPUTATIONAL METHODS IN ENGENEERING

Mechanical Analysis of Closed-Cell Foam Microbeams Using a High Order Beam Model Based on Modified Strain Gradient Theory

Fabio Carlos da Rocha[1], Elyakim Aguiar Santana[1], Leslie Darien Pérez Fernández[2], Julián Bravo Castillero[3], Maria do Socorro Martins Sampaio[4]

[1]*Dept. of Civil Engineering, Federal University of Sergipe*
Av. Marcelo Deda Chagas, 49107-230, São Cristóvão - SE, Brazil
fabiocrocha@academico.ufs.br, elyakim.aguiar.santana@gmail.com
[2]*Dept. of Mathematics and Statistics, Federal University of Pelotas*
Campus Universitário s/n, Prédio 5, 96160-000, Capãp do Leão - RS, Brazil
leslie.fernandez@ufpel.edu.br
[3]*IIMAS academic Unit at Yucatán, National Autonomous University of Mexico*
Car. Mérida-Tetiz, km 4.5, 97357, Ucú - YU, Mexico
julian@mym.iimas.unam.mx
[4]*Dept. of Civil Engineering, Amazonas State University*
Darcy Vargas Avenue, 69050-020, Manaus-AM, Brazil
msampaio@uea.edu.br

Abstract. Closed-cell foams are lightweight cellular materials widely used in applications that require high mechanical strength, low density, and excellent energy absorption capacity. These materials are used in impact absorption systems in the automotive industry, thermal and acoustic insulation in civil construction, structural components in the aerospace sector, biomedical prosthetics and implants, and functional elements in sensors, microactuators, and precision engineering devices. At the micro- and nanoscale, they are particularly relevant in the design of microbeams for emerging technologies. Due to scale effects that significantly influence the mechanical behavior of such structures, classical models become inadequate, necessitating the use of higher-order continuum theories for a more accurate representation. This study proposes a high-order laminated beam model based on the Modified Strain Gradient Theory, incorporating thickness-direction deformation (quasi-3D effect), a uniform distribution model for graphene nanoplatelets, and three distinct porosity distributions. The Halpin-Tsai model is employed to estimate the effective material properties. The governing differential equations and boundary conditions are derived through a variational approach, and the analytical solution is obtained using the Navier method. The results demonstrated excellent agreement with data from the literature, confirming the accuracy and robustness of the proposed model.

Keywords: Closed-cell foams, microbeams, strain gradient theory, porous materials, analytical modeling (up to 5 keywords)

1 Introduction

Metallic foams, especially those based on copper and aluminum, stand out for their low density, high specific stiffness, thermal performance, and energy absorption under low stress (Kulshreshtha and Dhakad [1]). This versatility enables the use of engineered foams with controlled porosity in functionally graded porous materials (FGPs) to optimize structural performance (D. Chen and Zhang [2], H. Rassoli and Temel [3], Keleshteri and Jelovica [4]).

Among recent nanoreinforcements, graphene nanoplatelets (GPLs) have emerged as highly effective, enabling improved mechanical, thermal, and electrical properties. More recently, GPL reinforced composites have been developed in functionally graded configurations (FG-GPLRC), with improved load tolerance and tunable through-thickness behavior (J. Yang and Kitipornchai [5], Z. Zhao and Yang [6], A. Lakel and Madan [7]).

The combination of FGP porous cores and GPLRC faces has resulted in advanced sandwich structures with superior mechanical performance. This combination mitigates issues like interfacial delamination and has been analyzed through analytical and numerical methods under bending, buckling, and vibration (W. Songsuwan and

Wattanasakulpong [8, 9]). Wattanasakulpong and Chaikittiratana [10] investigated the bending, buckling, and vibration responses of sandwich beams with FG-GPLRC faces and FGP cores using a generalized quasi-3D beam theory, showing that smooth or multilayered GPL and porosity distributions enhance structural performance and mechanical property continuity throughout the thickness of the beam.

To capture size-dependent behavior at the micro/nano scales, several non-classical continuum mechanics theories have been proposed (H. T. Thai and Kim [11]), including Modified Strain Gradient Theory (MSGT) introduced by D.C. Lam and Tong [12], which incorporates higher-order strain gradient metrics. Based on MSGT, the present study proposes a higher-order laminated beam model with transverse deformation (quasi-3D effect) and three porosity distributions. The effective material properties are estimated via the Halpin-Tsai model, and the governing equations and their boundary conditions are derived using a variational formulation. An analytical solution is obtained through the Navier method, which shows excellent agreement with the results of the literature, validating the accuracy and robustness of the model.

2 Mathematical Development

2.1 Kinematics and effective properties

Figure 1 shows a size-dependent simply supported beam with a porous core and faces reinforced with a uniformly dispersed pattern of graphene nanoplatelets (U-GPLRC), with the x and z axes representing the abscissa and ordinate axes, respectively. The beam has a total height h and length L, layer height h^k, and is subjected to a load $q(x)$.

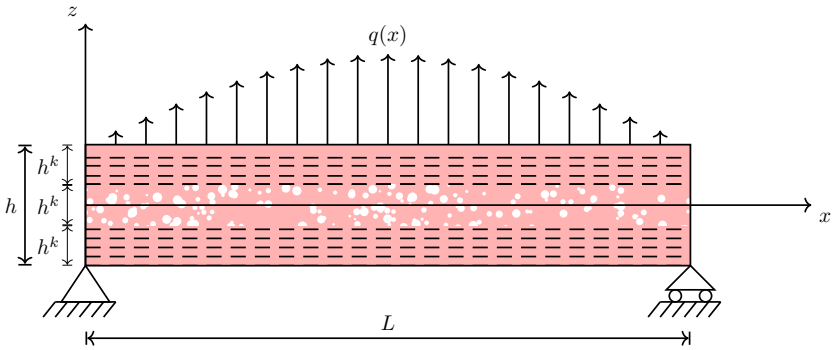


Figure 1. Beam with a porous core and faces U-GPLRC

The displacement field is expressed by eq. (1).

$$u_x^k(x,z) = u_0(x) - zw_{0,x} + f(z)\,\phi(x) + \Phi_{zz}^k(z)\,\psi(x),\ k = 1,...,N;\ u_z(x,z) = w_0(x) + g(z)\,\varphi(x), \quad (1)$$

where the comma denotes the differential operator; u_x^k and u_z represent the axial and transverse displacements, respectively. The indices k and N refer to the kth layer and the total number of layers, respectively. The axial displacement at the midplane of the beam is denoted by u_0, and the function $f(z) = z - \frac{4z^3}{3h^2}$ corresponds to high-order beam theory proposed by Reddy [13]. ϕ denotes the shear angle, and Φ_{zz}^k is the zigzag function, which can incorporate any admissible function, such as those adopted in this work [14–16]. The parameter ψ represents the amplitude of the zigzag function. The function $g(z)$, defined as the derivative of $f(z)$, accounts for transverse deformation (quasi-3D effect) and satisfies the transverse shear stress-free conditions on the upper and lower surfaces. Finally, φ is the unknown variable associated with the quasi-3D effect.

The material properties are determined according to the formulations presented in eqs. (2) to (4), corresponding to porosity distribution types 1, 2 and 3, respectively.

$$E^k(z) = E_1^k\left[1 - e_0^k\cos\left(\frac{\pi z}{h}\right)\right];\ \mu^k(z) = \frac{E^k(z)}{2\left[1+\nu^k(z)\right]};\ \rho^k(z) = \rho_1^k\left[1 - e_m^k\cos\left(\frac{\pi z}{h}\right)\right], \quad (2)$$

$$E^k(z) = E_1^k\left[1 - e_0^k \cos\left(\frac{\pi z}{2h} + \frac{\pi}{4}\right)\right];\ \mu^k(z) = \frac{E^k(z)}{2\left[1+\nu^k(z)\right]};\ \rho^k(z) = \rho_1^k\left[1 - e_m^k \cos\left(\frac{\pi z}{2h} + \frac{\pi}{4}\right)\right], \quad (3)$$

$$E^k = E_1^k \alpha^k;\ \mu^k = \frac{E^k}{2\left[1+\nu^k\right]};\ \rho^k = \rho_1^k \alpha'^k. \quad (4)$$

Here, E^k and μ^k denote the homogenized Young and shear moduli, respectively. The Young modulus of the FG-GPLRC is estimated using the Halpin-Tsai model E_1^k, while the Poisson's ratio is obtained from the closed-cell model proposed by Roberts and Garboczi [17] (eq. (6)). The coefficients e_0^k and e_m^k represent, respectively, the porosity and mass density, both for Type 1 and Type 2 distributions, whereas α^k and α'^k are the porosity parameters for the Type 3 distribution.

$$\begin{aligned} E_1^k &= \tfrac{3}{8}\tfrac{1+\xi_L^{GPL}\eta_L^k V_{GPL}^k}{1-\eta_L^k V_{GPL}^k} + \tfrac{5}{8}\tfrac{1+\xi_W^{GPL}\eta_W^k V_{GPL}^k}{1-\eta_W^k V_{GPL}^k} \\ \eta_L^k &= \frac{\left(E_{GPL}/E_m^k\right)-1}{\left(E_{GPL}/E_m^k\right)+\xi_{L(GPL)}^k};\ \eta_W^k = \frac{\left(E_{GPL}/E_m^k\right)-1}{\left(E_{GPL}/E_m^k\right)+\xi_{W(GPL)}^k} \\ \xi_L^{GPL} &= \tfrac{2L_{GPL}}{t_{GPL}};\ \xi_W^{GPL} = \tfrac{2W_{GPL}}{t_{GPL}}. \end{aligned} \quad (5)$$

The parameters ξ_L^{GPL}, η_L^k, ξ_W^{GPL}, and η_W^k depend on the GPL's geometric properties, length ($L_{GPL} = 2.5\mu m$), width ($W_{GPL} = 1.5\mu m$), and thickness ($t_{GPL} = 1.5nm$), as adopted in this work. The Young's modules of the GPL and the matrix are ($E_{GPL} = 1.01TPa$) and (E_m), respectively.

$$\nu^k(z) = 0.221\left(1 - \frac{\rho^k(z)}{\rho_1^k}\right) + \nu_1^k\left[0.342\left(1 - \frac{\rho^k(z)}{\rho_1^k}\right)^2 - 1.21\left(1 - \frac{\rho^k(z)}{\rho_1^k}\right) + 1\right], \quad (6)$$

where ν_1^k, ρ_1^k are determined using the rule of mixtures, and the volume fraction $V_{GPL}^k \in [0,1]$, associated with the uniformly distributed GPL pattern (U-GPLRC), is defined in eq. (7). In this expression, Λ_{GPL}^k denotes the GPL weight fraction, while $\rho_{GPL} = 1062.5kg/m^3$ and ρ_m^k are the mass densities of the GPL and matrix, respectively.

$$\nu_1^k = \nu_{GPL}^k V_{GPL}^k + \nu_m^k V_m^k;\ \rho_1^k = \rho_{GPL}^k V_{GPL}^k + \rho_m^k V_m^k;\ V_{GPL}^k = \frac{\Lambda_{GPL}^k}{\Lambda_{GPL}^k + \frac{\rho_{GPL}^k}{\rho_m^k}\left(1 - \Lambda_{GPL}^k\right)}, \quad (7)$$

2.2 Minimum total potential energy

The modified strain gradient elasticity theory (MSGT) D.C. Lam and Tong [12] is adopted to evaluate strain and stress in isotropic linear elastic materials. The corresponding strain energy U and external energy W are given by eq. (8).

$$U = \frac{1}{2}\int_\Omega \left(\sigma_{ij}\varepsilon_{ij} + p_i\gamma_i + \tau_{ijk}^{(1)}\eta_{ikk}^{(1)} + 2m_{ij}^s\chi_{ij}^s\right)dV;\ W = -\int_0^L \left(w_0(x) + g\left(\frac{h}{2}\right)\varphi(x)\right)q(x)\,dx, \quad (8)$$

where σ_{ij} is the classical stress tensor, while p_i, $\tau_{ijk}^{(1)}$ and m_{ij}^s are higher-order stresses. ε_{ij} denotes the strain tensor, γ_i dilatation gradient tensor, $\eta_{ijk}^{(1)}$ the deviatoric stretch gradient tensor, and χ_{ij}^s the symmetric rotation gradient tensor. The strain and stress fields are shown in eq. (9) and eq. (10), respectively.

$$
\begin{aligned}
&\varepsilon_{xx}^{k} = u_{0,x} - zw_{0,xx} + f\phi_{s,x} + \Phi_{zz}^{k}\psi_{,x};\ 2\varepsilon_{xz}^{k} = \left(f_{,z}\phi_s + \Phi_{zz,z}^{k}\psi + g\varphi_{,x}\right);\\
&\varepsilon_{zz} = g_{,z}\varphi;\ \gamma_{x}^{k} = u_{0,xx} - zw_{0,xxx} + f\phi_{s,xx} + \Phi_{zz}^{k}\psi_{,xx} + g_{,z}\varphi_{,x};\\
&\gamma_{z}^{k} = -w_{0,xx} + f_{,z}\phi_{s,x} + \Phi_{zz,z}^{k}\psi_{,x} + g_{,zz}\varphi;\\
&\eta_{xxx}^{(1)\,k} = \tfrac{1}{5}\left(2u_{0,xx} - 2zw_{0,xxx} + 2f\phi_{s,xx} + 2\Phi_{zz}^{k}\psi_{,xx} - f_{,zz}\phi_s - \Phi_{zz,zz}^{k}\psi - 2g_{,z}\varphi_{,x}\right);\\
&3\eta_{xxz}^{(1)\,k} = \tfrac{1}{5}\left(-4w_{0,xx} + 8f_{,z}\phi_{s,x} + 8\Phi_{zz,z}^{k}\psi_{,x} + 4g\varphi_{,xx} - 3g_{,zz}\varphi\right);\\
&3\eta_{xyy}^{(1)\,k} = \tfrac{1}{5}\left(-3u_{0,xx} + 3zw_{0,xxx} - 3f\phi_{s,xx} - 3\Phi_{zz}^{k}\psi_{,xx} - f_{,zz}\phi_s - \Phi_{zz,zz}^{k}\psi - 2g_{,z}\varphi_{,x}\right);\\
&3\eta_{xzz}^{(1)\,k} = \tfrac{1}{5}\left(4f_{,zz}\phi_s + 4\Phi_{zz,zz}^{k}\psi + 8g_{,z}\varphi_{,x} - 3u_{0,xx} + 3zw_{0,xxx} - 3f\phi_{s,xx} - 3\Phi_{zz}^{k}\psi_{,xx}\right);\\
&3\eta_{yyz}^{(1)\,k} = \tfrac{1}{5}\left(w_{0,xx} - 2f_{,z}\phi_{s,x} - 2\Phi_{zz,z}^{k}\psi_{,x} - g\varphi_{,xx} - 3g_{,zz}\varphi\right);\\
&\eta_{zzz}^{(1)\,k} = \tfrac{1}{5}\left(w_{0,xx} - 2f_{,z}\phi_{s,x} - 2\Phi_{zz,z}^{k}\psi_{,x} - g\varphi_{,xx} + 2g_{,zz}\varphi\right);\\
&2\chi_{xy}^{s\,k} = \tfrac{1}{2}\left(-g\varphi_{,xx} - 2w_{0,xx} + f_{,z}\phi_{s,x} + \Phi_{zz,z}^{k}\psi_{,x}\right);\ 2\chi_{yz}^{s\,k} = \tfrac{1}{2}\left(-g_{,z}\varphi_{,x} + f_{,zz}\phi_s + \Phi_{zz,zz}^{k}\psi\right),
\end{aligned}
\tag{9}
$$

$$
\begin{aligned}
&\sigma_{xx}^{k} = \left(\kappa^{k} - \tfrac{2}{3}\mu^{k}\right)\left(\varepsilon_{xx}^{k} + \varepsilon_{zz}\right) + 2\mu^{k}\varepsilon_{xx}^{k};\ 2\sigma_{xz}^{k} = 4\mu\varepsilon_{xz}^{k};\ \sigma_{yy}^{k} = \left(\kappa^{k} - \tfrac{2}{3}\mu^{k}\right)\left(\varepsilon_{xx}^{k} + \varepsilon_{zz}\right);\\
&\sigma_{zz}^{k} = \left(\kappa^{k} - \tfrac{2}{3}\mu^{k}\right)\left(\varepsilon_{xx}^{k} + \varepsilon_{zz}\right) + 2\mu^{k}\varepsilon_{zz};\ p_{x}^{k} = 2\mu^{k}(l_0^{k})^2\gamma_{x}^{k};\ p_{z}^{k} = 2\mu^{k}(l_0^{k})^2\gamma_{z}^{k};\\
&\tau_{xxx}^{(1)\,k} = 2\mu^{k}l_1^{2}\eta_{xxx}^{(1)\,k};\ 3\tau_{xzx}^{(1)\,k} = 6\mu^{k}(l_1^{k})^2\eta_{xzx}^{(1)\,k};\ 3\tau_{xyy}^{(1)\,k} = 6\mu^{k}(l_1^{k})^2\eta_{xyy}^{(1)\,k};\ 3\tau_{xzz}^{(1)\,k} = 6\mu^{k}(l_1^{k})^2\eta_{xzz}^{(1)\,k};\\
&3\tau_{yyz}^{(1)\,k} = 6\mu^{k}(l_1^{k})^2\eta_{yyz}^{(1)\,k};\ \tau_{zzz}^{(1)\,k} = 2\mu^{k}(l_1^{k})^2\eta_{zzz}^{(1)\,k};\ 2m_{xy}^{s\,k} = 4\mu^{k}(l_2^{k})^2\chi_{xy}^{s\,k};\ 2m_{yz}^{s\,k} = 4\mu^{k}(l_2^{k})^2\chi_{yz}^{s\,k},
\end{aligned}
\tag{10}
$$

where κ^k is the bulk modulus of the kth layer, given by $\kappa^k = \frac{E^k}{3(1-2\nu^k)}$. The parameters l_0^k, l_1^k and l_2^k denote the additional independent material length scale parameters.

By substituting Eq. eqs. (9) and (10) into eq. (8) and applying the minimum total potential energy principle, Euler's equations (eq. (12)) are obtained.

$$
\begin{aligned}
\delta u_0:\ & -A_3\varphi_{,x} - 2A_4u_{0,xx} + (-A_8 + A_{18})\phi_{s,xx} + (-A_{14} + A_{34})\psi_x\\
& - A_{21}w_{0,xxx} + A_{17}\varphi_{,xxx} + 2A_{19}u_{0,xxxx} + A_{32}\phi_{s,xxxx} + A_{38}\psi_{,xxxx} + A_{44}w_{0,xxxxx} = 0,\\
\delta\phi_s:\ & 2A_1\phi_s + (A_5 - A_7)\varphi_x + A_{10}\psi + (A_{18} - A_8)u_{0,xx} + 2(A_{31} - A_9)\phi_{s,xx}\\
& + (A_{37} - A_{15} + A_35)\psi_{,xx} + (A_{43} - A_{22})w_{0,xxx} + (-A_{25} + A_{30})\varphi_{,xxx}\\
& + A_{32}u_{0,xxxx} + 2A_{33}\phi_{s,xxxx} + A_{39}\psi_{,xxxx} + A_{45}w_{0,xxxxx} = 0,\\
\delta\psi:\ & A_{10}\phi_s + (A_{11} - A_{13})\varphi_{,x} + 2A_{12}\psi + (A_{34} - A_{14})u_{0,xx}\\
& + (A_{35} - A_{15} + A_{37})\phi_{s,xx} + 2(A_{40} - A_{16})\psi_{,xx} + (A_{46} - A_{23})w_{0,xxx}\\
& + (-A_{26} + A_{36})\varphi_{,xxx} + A_{38}u_{0,xxxx} + A_{39}\phi_{s,xxxx} + 2A_{41}\psi_{,xxxx} + A_{47}w_{0,xxxxx} = 0,\\
\delta w_0:\ & -2q(x) + A_{20}\varphi_{,xx} + A_{21}u_{0,xxx} + (A_{22} - A_{43})\phi_{s,xxx} + (A_{23} - A_{46})\psi_{,xxx}\\
& + 2A_{24}w_{0,xxxx} + (A_{28} - A_{42})\varphi_{,xxxx} - A_{44}u_{0,xxxxx} - A_{45}\phi_{s,xxxxx}\\
& - A_{47}\psi_{,xxxxx} - 2A_{48}w_{0,xxxxxx} = 0,\\
\delta\varphi:\ & -2g\left(\frac{h}{2}\right)q(x) + 2A_2\varphi + A_3u_{0,x} + (A_7 - A_5)\phi_{s,x} + (A_{13} - A_{11})\psi_x\\
& + A_{20}w_{0,xx} + 2(A_{27} - A_6)\varphi_{,xx} + (-A_{30} + A_{25})\phi_{s,xxx} + (-A_{36} + A_{26})\psi_{,xxx}\\
& - A_{17}u_{0,xxx} + (-A_{42} + A_{28})w_{0,xxxx} + 2A_{29}\varphi_{,xxxx} = 0.
\end{aligned}
\tag{11}
$$

Here, the terms A_i ($i \in \{1, \ldots, 48\}$) are given as follows:

$$
A_i = b\sum_{k=1}^{Nc}\int_{z_{k-1}}^{z_k}\sum_{m=1}^{M_i}\alpha_{im}\left(l_0^{k}, l_1^{k}, l_2^{k}, \kappa^{k}, \mu^{k}\right)\frac{d^{r_{im}}\eta_i(z)}{dz^{r_{im}}}\frac{d^{s_{im}}\eta_i^{*}(z)}{dz^{s_{im}}}dz. \tag{12}
$$

Table 1. Parameters composing the coefficients A_i in eq. (12)

A_i	$\eta_i(z)$	$\eta_i^*(z)$	M_i	(r_{i1}, s_{i1})	α_{i1}	(r_{i2}, s_{i2})	α_{i2}	A_i	$\eta_i(z)$	$\eta_i^*(z)$	M_i	(r_{i1}, s_{i1})	α_{i1}
1	f	f	2	$(1,1)$	$k_s\mu^k$	$(2,2)$	$\frac{1}{60}(32(l_1^k)^2+15(l_2^k)^2)\mu^k$	25	$f_{,z}$	g	1	$(0,0)$	$\frac{1}{30}(64(l_1^k)^2-15(l_2^k)^2)\mu^k$
2	g	g	2	$(1,1)$	$\kappa^k+\frac{4\mu^k}{3}$	$(2,2)$	$\frac{2}{5}(5(l_0^k)^2+2(l_1^k)^2)\mu^k$	26	$\phi^k_{zz,z}$	g	1	$(0,0)$	$\frac{1}{30}(64(l_1^k)^2-15(l_2^k)^2)\mu^k$
3	g	z	1	$(1,1)$	$\frac{2}{3}(3\kappa^k-2\mu^k)$	–	–	27	$g_{,zz}$	g	1	$(0,0)$	$-\frac{4}{5}(l_1^k)^2\mu^k$
4	1	1	1	$(0,0)$	$\kappa^k+\frac{4\mu^k}{3}$	–	–	28	g	1	1	$(0,0)$	$\frac{1}{15}(-16(l_1^k)^2+15(l_2^k)^2)\mu^k$
5	g	$f_{,z}$	2	$(0,0)$	$2k_s\mu^k$	$(1,1)$	$\frac{1}{30}(64(l_1^k)^2-15(l_2^k)^2)\mu^k$	29	g	g	1	$(0,0)$	$\frac{1}{60}(32(l_1^k)^2+15(l_2^k)^2)\mu^k$
6	g	g	2	$(0,0)$	$k_s\mu^k$	$(2,2)$	$\frac{1}{60}(120(l_0^k)^2+128(l_1^k)^2+15(l_2^k)^2)\mu^k$	30	$g_{,z}$	f	1	$(0,0)$	$\frac{4}{5}(5(l_0^k)^2-2(l_1^k)^2)\mu^k$
7	f	$g_{,z}$	2	$(0,0)$	$\frac{2}{3}(3\kappa^k-2\mu^k)$	$(1,1)$	$\frac{4}{5}(5(l_0^k)^2-2(l_1^k)^2)\mu^k$	31	$f_{,zz}$	f	1	$(0,0)$	$-\frac{4}{5}(l_1^k)^2\mu^k$
8	f	1	1	$(0,0)$	$\frac{2}{3}(3\kappa^k+4\mu^k)$	–	–	32	f	1	1	$(0,0)$	$\frac{4}{5}(5(l_0^k)^2+2(l_1^k)^2)\mu^k$
9	f	f	2	$(0,0)$	$\kappa^k+\frac{4\mu^k}{3}$	$(1,1)$	$\frac{1}{60}(120(l_0^k)^2+128(l_1^k)^2+15(l_2^k)^2)\mu^k$	33	f	f	1	$(0,0)$	$\frac{2}{5}(5(l_0^k)^2+2(l_1^k)^2)\mu^k$
10	f	ϕ^k_{zz}	2	$(1,1)$	$2k_s\mu^k$	$(2,2)$	$\frac{1}{30}(32(l_1^k)^2+15(l_2^k)^2)\mu^k$	34	$\phi^k_{zz,zz}$	1	1	$(0,0)$	$-\frac{4}{5}(l_1^k)^2\mu^k$
11	g	$\phi^k_{zz,z}$	2	$(0,0)$	$2k_s\mu^k$	$(1,1)$	$\frac{1}{30}(64(l_1^k)^2-15(l_2^k)^2)\mu^k$	35	$\phi^k_{zz,zz}$	f	1	$(0,0)$	$-\frac{4}{5}(l_1^k)^2\mu^k$
12	ϕ^k_{zz}	ϕ^k_{zz}	2	$(1,1)$	$k_s\mu^k$	$(2,2)$	$\frac{1}{60}(32(l_1^k)^2-15(l_2^k)^2)\mu^k$	36	ϕ^k_{zz}	$g_{,z}$	1	$(0,0)$	$\frac{4}{5}(5(l_0^k)^2-2(l_1^k)^2)\mu^k$
13	ϕ^k_{zz}	$g_{,z}$	2	$(0,0)$	$\frac{2}{3}(3\kappa^k-2\mu^k)$	$(1,1)$	$\frac{4}{5}(5(l_0^k)^2-2(l_1^k)^2)\mu^k$	37	ϕ^k_{zz}	$f_{,zz}$	1	$(0,0)$	$-\frac{4}{5}(l_1^k)^2\mu^k$
14	ϕ^k_{zz}	1	1	$(0,0)$	$\frac{2}{3}(3\kappa^k+4\mu^k)$	–	–	38	ϕ^k_{zz}	1	1	$(0,0)$	$\frac{4}{5}(5(l_0^k)^2+2(l_1^k)^2)\mu^k$
15	f	ϕ^k_{zz}	2	$(0,0)$	$\frac{2}{3}(3\kappa^k+4\mu^k)$	$(1,1)$	$\frac{1}{30}(120(l_0^k)^2+128(l_1^k)^2+15(l_2^k)^2)\mu^k$	39	ϕ^k_{zz}	f	1	$(0,0)$	$\frac{4}{5}(5(l_0^k)^2+2(l_1^k)^2)\mu^k$
16	ϕ_{zz}	ϕ_{zz}	2	$(0,0)$	$\kappa^k+\frac{4\mu^k}{3}$	$(1,1)$	$\frac{1}{60}(120(l_0^k)^2+128(l_1^k)^2+15(l_2^k)^2)\mu^k$	40	ϕ^k_{zz}	$\phi^k_{zz,zz}$	1	$(0,0)$	$-\frac{4}{5}(l_1^k)^2\mu^k$
17	$g_{,z}$	1	1	$(0,0)$	$\frac{4}{5}(5(l_0^k)^2-2(l_1^k)^2)\mu^k$	–	–	41	ϕ^k_{zz}	ϕ^k_{zz}	1	$(0,0)$	$\frac{2}{5}(5(l_0^k)^2+2(l_1^k)^2)\mu^k$
18	f	$\frac{z^2}{2}$	1	$(2,2)$	$-\frac{4}{5}(l_1^k)^2\mu^k$	–	–	42	z	$g_{,z}$	1	$(0,0)$	$\frac{4}{5}(-5(l_0^k)^2+2(l_1^k)^2)\mu^k$
19	1	1	1	$(0,0)$	$(2(l_0^k)^2+\frac{4}{5}(l_1^k)^2)\mu^k$	–	–	43	z	$f_{,zz}$	1	$(0,0)$	$\frac{4}{5}(l_1^k)^2\mu^k$
20	$\frac{z^2}{2}$	g	2	$(1,1)$	$\frac{2}{3}(-3\kappa^k+2\mu^k)$	$(2,2)$	$\frac{4}{5}(-5(l_0^k)^2+(l_1^k)^2)\mu^k$	44	z	1	1	$(0,0)$	$-\frac{4}{5}(5(l_0^k)^2+2(l_1^k)^2)\mu^k$
21	z	1	1	$(0,0)$	$-\frac{2}{3}(3\kappa^k+4\mu^k)$	–	–	45	z	f	1	$(0,0)$	$-\frac{4}{5}(5(l_0^k)^2+2(l_1^k)^2)\mu^k$
22	z	f	2	$(0,0)$	$-\frac{2}{3}(3\kappa^k+4\mu^k)$	$(1,1)$	$-\frac{1}{15}(60(l_0^k)^2+32(l_1^k)^2+15(l_2^k)^2)\mu^k$	46	z	ϕ^k_{zz}	1	$(0,0)$	$\frac{4}{5}(l_1^k)^2\mu^k$
23	z	ϕ^k_{zz}	2	$(0,0)$	$-\frac{2}{3}(3\kappa^k+4\mu^k)$	$(1,1)$	$-\frac{1}{15}(60(l_0^k)^2+32(l_1^k)^2+15(l_2^k)^2)\mu^k$	47	z	ϕ^k_{zz}	1	$(0,0)$	$-\frac{4}{5}(5(l_0^k)^2+2(l_1^k)^2)\mu^k$
24	z	z	2	$(0,0)$	$\kappa^k+\frac{4\mu^k}{3}$	$(1,1)$	$(2(l_0^k)^2+\frac{8}{15}(l_1^k)^2+(l_2^k)^2)\mu^k$	48	z	z	1	$(0,0)$	$\frac{2}{5}(5(l_0^k)^2+2(l_1^k)^2)\mu^k$

2.3 Analytical solution

The Navier procedure was used to solve the differential equations in eq. (12), approximating the response fields by periodic functions with separated variables. Furthermore, the uniformly distributed load $q(x)$ was represented by Fourier series. For a simply supported beam, the boundary conditions are defined by $w(0) = w(L) = 0$, which corresponds to the imposition of zero deflection on the supports, that is, at both ends of the beam, where the vertical displacements are zero and the solution is expressed as in eq. (13).

$$\begin{aligned} u_0(x) &= \sum_{n=1}^{NT} u_{0_i} \cos\left(\tfrac{n\pi x}{L}\right), \phi_s(x) = \sum_{n=1}^{NT} \phi_{s_i} \cos\left(\tfrac{n\pi x}{L}\right), \psi(x) = \sum_{n=1}^{NT} \psi_i \cos\left(\tfrac{n\pi x}{L}\right), \\ w_0(x) &= \sum_{n=1}^{NT} w_{0_i} \sin\left(\tfrac{n\pi x}{L}\right), \varphi(x) = \sum_{n=1}^{NT} \varphi_i \sin\left(\tfrac{n\pi x}{L}\right), q(x) = \tfrac{4q_0}{j\pi} \sin(\tfrac{j\pi x}{L})\ j = 1,3,5,... \end{aligned} \tag{13}$$

where NT represents the number of terms in the series. The coefficiente u_{0_i}, ϕ_i, ψ_i, w_{0_i} and φ_i are determined by substituting eq. (13) into eq. (12) and solving the resulting system of algebraic system.

2.4 Results and discussions

A sandwich microbeam subjected to a uniformly distributed load is analyzed, where the outer layers consist of copper uniformly reinforced with graphene nanoplatelets (Cu + GPL) and the core is copper metal foam (Cu + porous). The beam is assumed to have length L, with equal layer depths $h^1 = h^2 = h^3 = \frac{1}{3}h$, where the total depth is $h = 1$. The width is b = h, and the aspect ratio is $L/h = 10$. The volume fraction of graphene nanoplatelets in the outer layers is $\Lambda^1_{GPL} = \Lambda^3_{GPL} = 0.01$. The core of copper metal foam has the porosity parameter $e_0 = 0.5$ for the symmetric (Type 1) and asymmetric (Type 2) pore distributions, and $\alpha = 0.6722$ for the uniform distribution model (Type 3), all with equivalent mass density. The metallic matrix common to all layers has elastic modulus $E_m = 130GPa$, Poisson ratio $\nu_m = 0.34$, and density $\rho_m = 8960kg/m^3$. The maximum deflections shown in Table 2 are normalized according to: $|w| = \frac{100E_m bh^3}{q_0 L^4} u_z(\frac{L}{2}, 0)$.

Table 2 presents the deflection values reported by [10], obtained using an advanced beam model (RED) from Reddy [13] that incorporates quasi-3D (Q3D) effects in its kinematic formulation, together with the plane stress constitutive model.

Table 2. Maximum deflection for a sandwich beam with faces (Cu + U-GPLRC) and copper foam core

Porous distribution	**[10]***	**PW*** ($l = 0$)	**PW**** ($l = 0$)	**PW**** ($l = 0.5h^k$)	**PW**** ($l = h^k$)	**PW**** ($l = 2h^k$)
Type 1						
REDQ3D	10.7514	10.7484	9.6233	7.6637	4.7717	1.9080
RED	9.6588	9.6559	7.4488	5.8917	3.6290	1.4341
REDQ3DMUR	–	10.7951	9.6698	7.6685	4.7843	1.9713
REDQ3DZHEN	–	10.8046	9.6793	7.7371	4.8499	1.9693
REDQ3DZZHE	–	10.7949	9.6697	7.7218	4.8199	1.9291
Type 2						
REDQ3D	10.7786	10.7757	9.6479	7.6799	4.7785	1.9093
RED	9.6838	9.6809	7.4692	5.9053	3.6347	1.4351
REDQ3DMUR	–	10.8206	9.6926	7.6844	4.7914	1.9728
REDQ3DZHEN	–	10.8309	9.7028	7.7522	4.8556	1.9701
REDQ3DZZHE	–	10.8255	9.6975	7.7397	4.8269	1.9302
Type 3						
REDQ3D	10.7880	10.7850	9.6572	7.6887	4.7853	1.9126
RED	9.6930	9.6900	7.4790	5.9136	3.6405	1.4377
REDQ3DMUR	–	10.8301	9.7029	7.6933	4.7983	1.9769
REDQ3DZHEN	–	10.8417	9.7138	7.7622	4.8631	1.9734
REDQ3DZZHE	–	10.8373	9.7093	7.7499	4.8340	1.9335

*Present Work (**PW**); * Plane Stress ; ** Plane Strain*

In addition, the table includes results obtained with the kinematics proposed in the present work (PW), employing the same PT constitutive model as [10], but neglecting the zigzag (ZZ) effect by setting $\Phi^k_{zz} = 0$.

Furthermore, the table shows the deflections corresponding to the complete model proposed here, which combines unified kinematics with the Q3D effect and enriches ZZ functions as introduced by [14–16] (MUR, ZHEN, and ZZHE, respectively). These results consider both the classical continuum theory $l^k_0 = l^k_1 = l^k_2 = 0$ and the strain gradient theory $l^k_0 = l^k_1 = l^k_2 = l$ under a plane strain assumption.

When using the plane stress constitutive model combined with the unified kinematic formulation developed in this study, the results exhibit good agreement with those reported by [10]. Conversely, employing the constitutive model proposed in this plane strain study without accounting for micromechanical effects leads to smaller deflections, consistent with the increased stiffness inherent to the adopted modeling approach.

A clear relationship between the parameters l^k_0, l^k_1, and l^k_2 and the layer depth h^k is observed in Table 2. As these relationships increase relative to h^k, an apparent increase in flexural stiffness occurs. Conversely, as the relationship values approach zero, the stiffness tends to converge to that predicted by classical continuum theory. Among the porosity distribution models in the central layer of the sandwich microbeam, the uniform distribution exhibited slightly higher deflections compared to other models. However, it was observed that the choice of porosity distribution had minimal influence on the deflection results.

Additionally, when considering the zigzag kinematic models (REDQ3DMUR, REDQ3DZHEN, and REDQ3DZZHE), the sensitivity of the deflection results was also small. This limited influence of the ZZ models is attributed to the relatively high L/h ratio employed in this analysis.

3 Conclusions

The beam model developed in this work, based on unified kinematics, strain gradient theory, and higher-order zigzag theories, proved effective both in reproducing results from the literature and in comparing beam theories coupled with zigzag models and with quasi-3D effects. In the analysis of micromechanical effects, the length scale parameter significantly influenced flexural stiffness, demonstrating the scale effect. Furthermore, for the aspect ratio L/h=10, the influence of pore distribution in the copper foam core, combined with copper faces reinforced with uniformly dispersed GPL, was shown to have little effect on deflection values. Preliminary studies in progress, although not presented in this work, suggest that for lower values of the L/h ratio, the type of zigzag function and the porosity distribution exert a moderate influence on the results, indicating the need for further investigation of these variables.

Acknowledgements. The authors acknowledge the financial support from FAPITEC/SE/FUNTEC and CAPES. E.A.S. acknowledges the master's scholarship from FAPITEC; J.B.C. acknowledges support from CAPES through the PRAPG program (Grant 23038.003836/2023-39); and F.C.R. acknowledges support through the Universal Project (Grant 019203.01702/2024-6) and FAPITEC/SE/FUNTEC-PRAPEC (Call No. 05/2025).

Authorship statement. The authors hereby confirm that they are the sole liable persons responsible for the authorship of this work, and that all material that has been herein included as part of the present paper is either the property (and authorship) of the authors, or has the permission of the owners to be included here.

References

[1] A. Kulshreshtha and S. K. Dhakad. Preparation of metal foam by different methods: A review. *Materials Today: Proceedings*, vol. 26, n. 1, pp. 1784–1790, 2020.
[2] J. Y. K. Gao. D. Chen and L. Zhang. Functionally graded porous structures: analyses, performances, and applications–a review. *Thin-Walled Structures*, vol. 191, n. 1, pp. 111046, 2023.
[3] A. R. N. H. Rassoli and B. Temel. Static analysis of functionally graded porous beam-column frames by the complementary functions method. *Structures*, vol. 62, n. 1, pp. 106136, 2024.
[4] M. M. Keleshteri and J. Jelovica. Analytical assessment of nonlinear forced vibration of functionally graded porous higher order hinged beams. *Composite Structures*, vol. 298, n. 1, pp. 115994, 2024.
[5] H. W. J. Yang and S. Kitipornchai. Buckling and postbuckling of functionally graded multilayer graphene platelet-reinforced composite beams. *Composite Structures*, vol. 161, n. 1, pp. 111–118, 2017.
[6] Y. D. Y. W. C. Feng. Z. Zhao and J. Yang. Geometrically nonlinear bending of functionally graded nanocomposite trapezoidal plates reinforced with graphene platelets (gpls). *International Journal of Mechanics and Materials in Design*, vol. 15, n. 4, pp. 791–800, 2019.
[7] M. A. H. A. A. L. Hadji. A. Lakel and R. Madan. The natural frequency analysis of fg-gnpr nanoplates under different boundary conditions. *Advances in nano research*, vol. 17, n. 6, pp. 533–546, 2024.
[8] C. P. W. Songsuwan and N. Wattanasakulpong. On linear and nonlinear bending of functionally graded graphene nanoplatelet reinforced composite beams using gram-schmidt-ritz method. *Mechanics Based Design of Structures and Machines*, vol. 51, n. 10, pp. 5710–5736, 2023.
[9] C. P. W. Songsuwan and N. Wattanasakulpong. Nonlinear bending of elastically restrained functionally graded graphene nanoplatelet reinforced beams with an open edge crack. *Thin-Walled Structures*, vol. 156, n. 1, pp. 106972, 2020.
[10] N. Wattanasakulpong and A. Chaikittiratana. A comprehensive study on bending, buckling and vibration of sandwich beams made of fg-gplrc faces and fgp core using a quasi-3d theory. *Structures*, vol. 74, n. 1, pp. 108561, 2025.
[11] T. K. N. T. P. Vo. H. T. Thai and S. E. Kim. A review of continuum mechanics models for size-dependent analysis of beams and plates. *Composite Structures*, vol. 177, n. 1, pp. 196–219, 2017.
[12] A. C. M. C. J. W. F. Yang. D.C. Lam and P. Tong. Experiments and theory in strain gradient elasticity. *Journal of the Mechanics and Physics of Solids*, vol. 51, n. 8, pp. 1477–1508, 2003.
[13] J. Reddy. A general non-linear third-order theory of plates with moderate thickness. *International Journal of Non-Linear Mechanics*, vol. 25, n. 6, pp. 677–686, 1990.
[14] H. Murakami. Laminated composite plate theory with improved in-plane responses. *Journal Applied Mechanics*, vol. 53, n. 3, pp. 661–666, 1986.
[15] H. Z. C. Yang. W. Zhen and X. Zheng. Stability of laminated composite and sandwich beams by a reddy-type higher-order zig-zag theory. *Mechanics of Advanced Materials and Structures*, vol. 26, n. 19, pp. 1622–1635, 2019.
[16] L. P. Leite and da F. Rocha. A novel exponential zigzag function coupled high-order beam theory for advanced laminated composite analysis. *Journal of Applied and Computational Mechanics*, vol. 10, n. 2, pp. 330–341, 2024.
[17] A. P. Roberts and E. J. Garboczi. Computation of the linear elastic properties of random porous materials with a wide variety of microstructure. proceedings of the royal society of london. *Proceedings of the Royal Society of London. Series A: Mathematical, Physical and Engineering Sciences*, vol. 458, n. 2021, pp. 1033–1054, 2002.